Selective segmentation of brain abnormalities in colour MRI images using variational model

Akmal Shafiq Badarul Azam[1], Abdul Kadir Jumaat[2,4*], Shafaf Ibrahim[3], Nor Farihah Azman[2], Sarah Farhana Zamalik[1], Muhammad Zulkhairi Zakariah[1]

[1]*School of Mathematical Sciences, College of Computing, Informatics and Mathematics, Universiti Teknologi MARA Sarawak Branch, Mukah Campus, Mukah, Malaysia*
[2]*School of Mathematical Sciences, College of Computing, Informatics and Mathematics, Universiti Teknologi MARA Shah Alam, Selangor, Malaysia*
[3]*School of Computing Sciences, College of Computing, Informatics and Mathematics, Universiti Teknologi MARA Shah Alam, Selangor, Malaysia*
[4]*Institiute for Big Data Analytics and Artificial Intelligence (IBDAAI), Universiti Teknologi MARA Shah Alam, Selangor, Malaysia*

ARTICLE INFO	ABSTRACT
	Early detection of brain abnormalities is vital for enhancing patient outcomes and survival rates. However, accurately identifying and segmenting these abnormalities from MRI images remains a persistent challenge. This study assesses the efficacy of the Selective Local Image Fitting (SLIF) model in segmenting brain abnormalities from colour MRI images and compares its performance with converted greyscale counterparts. The rationale behind this comparison stems from standard practice in image segmentation, where colour images are often converted to greyscale before the segmentation task. Converting the image might degrade data by diminishing its dimensions, potentially affecting segmentation computations. This study intends to evaluate the influence of colour information on segmentation accuracy and efficiency by directly assessing the SLIF model on both colour and converted greyscale images. Segmentation accuracy was evaluated using metrics such as the Dice Similarity Coefficient (DSC), Matthews Correlation Coefficient (MCC), and Intersection-over-Union (IoU). Efficiency was determined by measuring the average elapsed processing time. Experimental results demonstrate that colour MRI brain images outperform their converted greyscale counterparts in segmentation accuracy, as colour providing essential supplementary information for precise abnormality delineation. Despite a slight increase in average elapsed processing time for colour images, the enhanced accuracy justifies this trade-off. These findings emphasize the importance of colour MRI in enhancing diagnostic accuracy, especially in detecting

[2*] Corresponding author. *E-mail address:* abdulkadir@tmsk.uitm.edu.my

brain abnormalities. This study can be extended in future work to evaluate the segmentation accuracy and efficiency of brain abnormalities in 3D colour and greyscale MRI images.

1.   INTRODUCTION

Significant breakthroughs have been made in combating various diseases due to recent advancesin biological research and human intelligence. However, cancer remains a substantial challenge because of its inherently unpredictable nature [1]. In 2022, the International Agency for Research on Cancer (IARC) reported 321,476 newly diagnosed cases of brain and neurological system cancer. This form of cancer was ranked nineteenth among all types of cancer in terms of occurrence. Furthermore, there were 248,305 confirmed deaths globally, making brain and neurological system cancers the twelfth most prevalent cause of cancer-related deaths [2]. Brain abnormalities encompass deviations from typical brain function, structure or biochemical levels. They stem from various causes, such as genetic mutations, complications during childbirth, developmental disorders or trauma, exposure to harmful substances, and diseases affecting the mother or the developing fetus. These abnormalities are associated with conditions such as schizophrenia, autism, various types of brain tumours, alcohol addiction and dementia [3].

Radiologists have employed a range of medical imaging techniques, such as X-ray, computed tomography (CT), magnetoencephalography, magnetic resonance imaging (MRI), electroencephalography, ultrasound, and positron emission tomographic (PET), to identify and analyse brain abnormalities. Out of these options, MRI is considered the most favourable due to its non-intrusive characteristics, lack of radiation from ions, and capacity to offer extensive details about the brain's state, whether healthy or impacted by disease [4]. However, segmenting MRI brain abnormalities remains challenging due to variations in intensity across images, low contrast, and other imaging inconsistencies [5].

Brain abnormalities segmentation involves distinguishing abnormal areas within the brain from the normal background. Segmentation algorithms for brain abnormalities are rapidly advancing in accuracy and speed through the integrationof new theories and technologies [6]. However, there is still significant room for improvement and many challenges that require further investigation and research related to this area. These segmentation models are classified into two categories: variational segmentation (level-set) and non-variational segmentation (non-level set). Variational segmentation models minimise cost-energy functions using the theory of variational calculus, applying optimisation algorithms to attain optimality. Conversely, heuristic techniques develop non-variational methods [7-8].

A wealth of research has been conducted on non-variational segmentation models for MRI brain abnormalities, encompassing diverse approaches such as the Fast Fuzzy C-means algorithm [9], clustering-based algorithms [10] and deep neural networks [11]. Additionally, learning-based approaches, notably deep learning techniques like the Attention U-Net model [12], have gained popularity in MRI brain segmentation. The focus promising outcomes drive the focus on learning-based approaches. However, achieving accurate generalisation to new images requires extensive and varied training datasets. Inadequate training data may cause these methods to falter when faced with images exhibiting significant deviations from the training distribution. Moreover, this approach can yield opaque decisions that pose challenges for interpretation [13].

Hence, numerous researchers aim to devise variational segmentation models that demand less data for image segmentation while delivering remarkable speed and accuracy in results. Global variational segmentation and selective variational segmentation are the two primary forms of variational segmentation approaches that can be distinguished in their approach to extracting information from an input image. Selective variational segmentation focuses on extracting regions of interest based on geometrical constraints, while global variational segmentation aims to determine the borders of all objects inside the image [14]. In 2017, [15] devised a level-set approach to segment greyscale MRI brain segmentation. They

addressed challenges such as noise and uneven intensity by integrating a local Gaussian distribution to handle intensity inhomogeneity and implementing a bias field correction technique to enhance accuracy. Subsequently, [16] proposed another method for greyscale MRI brain segmentation using Gaussian distributions to model image intensities, specifically aimed at segmenting brain lesions in MRI with intensity inhomogeneity. Indeed, both models are solely tailored for global segmentation, which can lead to suboptimal results when abnormal regions have intensities nearly identical to healthy tissue, are situated close to healthy tissue boundaries, have indistinct contours, suffer from low contrast, or are affected by noise [17].

A selective variational segmentation model is preferred to segment a particular object given an input image. [18] introduced a selective variational segmentation model for greyscale medical images including brain images, that integrate saliency maps and local image fitting techniques. Saliency maps highlight the most visually distinct portions of an image, enhancing the model's ability to focus on important segments. The local image fitting component improves segmentation by adjusting the local intensity variations, increasing the model's precision. This model was tested on 30 medical images including brain MRI scans, and demonstrated significant improvements over existing models. Another related research on selective segmentation models for brain images was proposed by [19-21]. Nevertheless, all these models are only relevant to greyscale MRI brain images.

To achieve better results by incorporating more information, the use of colour information can enhance feature extraction and improve boundary detection [5]. [12] introduced a new model that utilises deep neural networks to segment colour MRI brain abnormalities. This approach combines the Attention U-Net architecture with a hybrid loss function based on active contour. The Attention U-Net improves segmentation accuracy by directing the model's focus to relevant regions using attention mechanisms. The hybrid loss function, which combines binary cross-entropy with the traditional greyscale Chan-Vese global model, ensures that the abnormality boundaries are precisely delineated. This combination improves performance in accurately recognising and segmenting brain abnormalities. Despite these promising results, this method is needed for larger, more diversified datasets and computational capacities to segment more colour MRI brain abnormalities images.

On top of that, a new selective variational for colour images, named the Selective Local Image Fitting (SLIF) model was proposed by [22]. This model is specifically developed to partition vector-valued (colour) images that exhibit variations in intensity. It incorporates local image fitting concepts from the Local Image Fitting (LIF) model by [23] and integrates a distance fitting term from the Distance Selective Segmentation 2 (DSS2) model by [24] into the colour variational energy functional framework to effectively and selectively segment colour images with intensity inhomogeneity. The SLIF model also employs a Gaussian function for curve regularisation. Numerical studies provided empirical evidence that the suggested SLIF model effectively segmented the region of interest in vector-valued images, yielding superior segmentation outcomes compared to the previous methods. This superiority was notably evident in synthetic, medical, and natural images. However, this model has not yet been tested on colour MRI brain abnormalities. It is important to note that segmenting colour MRI brain abnormalities is particularly challenging to the complexity of differentiating abnormal tissue from normal tissue, the presence of intensity inhomogeneity, low image contrast, and variability of brain structures.

Thus, this paper aims to evaluate the effectiveness of the SLIF model in segmenting brain abnormalities in colour MRI images. Additionally, we are interested in comparing the segmentation performance between colour MRI images and their converted greyscale counterparts to explore the trade-off between accuracy and efficiency when using a variational active contour model. The rationale for this comparison lies in the prevalent practice of converting colour images to greyscale before segmentation. Such conversion may lead to data loss due to reduced image dimensions, potentially impacting the performance of segmentation algorithm. It is worth noting that, although the SLIF model is primarily intended for colour images, it may also be used to segment greyscale images by first converting the colour MRI images into greyscale. When

processing images, the SLIF model treats colour images as having three layers (one for each colour channel: red, green, and blue), whereas it considers greyscale images as having only one layer. The subsequent sections of this work are organised as follows: Section 2 reviews related works, including the foundational models LIF, DSS2, and SLIF. Section 3 outlines the methodology employed in this research, while Section 4 showcases the experimental results and subsequent discussion. Section 5 concludes and offers recommendations.

2.   RELATED WORKS

This section provides an overview of the Local Image Fitting (LIF) model, the Distance Selective Segmentation 2 (DSS2) model, and the Selective Local Image Fitting (SLIF) model.

2.1   Local image fitting (LIF) model

The Local Image Fitting (LIF) model, introduced by [23], has gained significant recognition in the field. This model effectively addresses the challenges associated with images exhibiting varying intensity levels and improves segmentation speed. It achieves this by evaluating the disparities between the original greyscale image and a locally fitted version. Assume that for an image $u = u(x, y)$ in a domain Ω, the regularised local image fitting energy functional in the level set formulation is expressed in Eq. (1):

$$E_{\varepsilon}^{LIF}(\phi) = \frac{1}{2} \int_{\Omega} \left| u - n_1 H_{\varepsilon}(\phi) + n_2 \left(1 - H_{\varepsilon}(\phi)\right) \right|^2 dxdy \,. \tag{1}$$

Here, n_1 and n_2 represent the intensity averages of the interior and exterior within a local region, defined using a truncated Gaussian window $W_k(x, y)$, with a standard deviation σ and a kernel window with a radius k. These constants are defined in Eq. (2):

$$
\begin{aligned}
n_1 &= mean\left(u \in \left(\{(x, y) \in \Omega \mid \phi(x, y) > 0\} \cap W_k(x, y)\right)\right) \\
n_2 &= mean\left(u \in \left(\{(x, y) \in \Omega \mid \phi(x, y) < 0\} \cap W_k(x, y)\right)\right)
\end{aligned}
\tag{2}
$$

Then, applying the variational calculus and the steepest descent method on Eq. (1) leads to:

$$\frac{d\phi}{dt} = \left(u - n_1 H_{\varepsilon}(\phi) - n_2 \left(1 - H_{\varepsilon}(\phi)\right)\right)\left(n_1 - n_2\right)\delta_{\varepsilon}(\phi)\,, \tag{3}$$

where $H_{\varepsilon}(\phi) = 0.5\left(1 + \left(2/\pi\right)\arctan\left(\phi/\varepsilon\right)\right)$ is the regularised form of the Heaviside function and $\delta_{\varepsilon}(\phi) = \varepsilon / \left(\pi\left(\varepsilon^2 + \phi^2\right)\right)$ is the Dirac delta function. Additionally, incorporating a Gaussian function for variational level set regularisation can eliminate the need to solve the highly non-linear curvature term $\nabla.\left(\nabla\phi / |\nabla\phi|\right)$, which is computationally expensive. This, in turn, reduces the overall computational complexity.

The widespread adoption of the LIF model and the Gaussian function among researchers is a testament to their effectiveness in segmenting images with varying intensity levels [25-26]. However, these models,

including the LIF model, are unsuitable for colour images and selective segmentation. They tend to produce over-segmented results when the region of interest (foreground) has intensities that are nearly identical to those of the background [20].

2.2 Distance selective segmentation 2 (DSS2) model

The Distance Selective Segmentation 2 (DDS2), introduced by [17], is a selective segmentation model designed for colour images. Assume that, for an image $u = u(x, y)$, there are m_1 geometrical points that must be close to the desired object boundary, forming a marker set β, which is provided by the user as follows (Eq. (4)):

$$\beta = \left\{ w_j = (x_j^*, y_j^*) \in \Omega, \ 1 \le j \le m_1 \right\} \subset \Omega , \tag{4}$$

where $m_1 \ge 3$ will connect the markers to form an initial polygon P that drives its evolution towards a curve Γ. Then, the function $L_d(x, y)$ expressed as the Euclidean distance of each point $(x, y) \in \Omega$ from its closest point $(x_p, y_p) \in P$ is given by Eq. (5):

$$L_d(x, y) = \left[(x - x_p)^2 + (y - y_p)^2 \right]^{\frac{1}{2}} = \min_{p \in P} \| (x, y) - (x_p, y_p) \| . \tag{5}$$

By applying the level set function ϕ, the DSS2 energy functional is then defined as in Eq. (6):

$$\min_{\phi, \overline{k_1}, \overline{k_2}} \left\{ E_\varepsilon^{DSS2} \left(\phi, \overline{k_1}, \overline{k_2} \right) = \mu \int_\Omega |\nabla H_\varepsilon(\phi)| \, dxdy + \int_\Omega \theta H_\varepsilon(\phi) L_d(x, y) dxdy \right. $$
$$+ \int_\Omega \frac{1}{N} \sum_{i=1}^{N} \lambda_1 \left(u^i - k_1^i \right)^2 H_\varepsilon(\phi) dxdy \tag{6}$$
$$\left. + \int_\Omega \frac{1}{N} \sum_{i=1}^{N} \lambda_2 \left(u^i - k_2^i \right)^2 \left(1 - H_\varepsilon(\phi) \right) dxdy \right\}$$

where $u^i = u^i(x, y)$ is the ith channel of an image on Ω with $i = 1, 2, ..., N$ channels. Additionally, $\overline{k_1} = \left(k_1^1, ..., k_1^N \right)$ and $\overline{k_2} = \left(k_2^1, ..., k_2^N \right)$ are intensity averages of interior and exterior in a global region. The non-negative parameters $\mu > 0$ $\lambda_1 > 0$ and $\lambda_2 > 0$ are weights for the regularising and fitting terms, respectively. The area parameter θ helps determine the weight of the distance fitting term. The regularised Heaviside function $H_\varepsilon(\phi)$ and the Dirac delta function $\delta_\varepsilon(\phi)$ are defined as in Eq. (7) and Eq. (8):

$$H_\varepsilon(\phi) = \begin{cases} 1 \text{ if } \phi > \varepsilon \\ 0 \text{ if } \phi < \varepsilon \\ 0.5 \left[1 + (\phi / \varepsilon) + (1 / \pi) \sin (\pi\phi / \varepsilon) \right] \text{ if } |\phi| \le \varepsilon \end{cases} , \tag{7}$$

and

$$\delta_\varepsilon(\phi) = \frac{1}{2\varepsilon}\left[1 + \cos\left(\frac{\pi\phi}{\varepsilon}\right)\right] \text{ if } |\phi| \le \varepsilon . \tag{8}$$

Let the level set function ϕ be fixed. Then, Eq. (6) was minimised with respect to k_1^i and k_2^i that yielded the following Eq. (9):

$$
\begin{aligned}
k_1^i(\phi) &= \frac{\int_\Omega u^i(x,y)H_\varepsilon(\phi)dxdy}{\int_\Omega H_\varepsilon(\phi)dxdy}, & \left(average\left(u^i\right) \text{ on } \phi \ge 0\right) \\
k_2^i(\phi) &= \frac{\int_\Omega u^i(x,y)\left(1-H_\varepsilon(\phi)\right)dxdy}{\int_\Omega H_\varepsilon(\phi)dxdy}, & \left(average\left(u^i\right) \text{ on } \phi < 0\right)
\end{aligned}
\tag{9}
$$

Fixing k_1^i and k_2^i as constants lead to the following Euler-Lagrange equations as follows (Eq. (10)):

$$
\begin{cases}
\delta_\varepsilon(\phi)\left[\mu\nabla.\left(\frac{\nabla\phi}{|\nabla\phi|}\right) - \theta F_d - \frac{1}{N}\sum_{i=1}^N\left(\lambda_1\left(u^i - k_1^i\right)^2 - \lambda_2(u^i - k_2^i)^2\right)\right] = 0, & \text{in } \Omega \\
\frac{\delta_\varepsilon(\phi)}{|\nabla\phi|}\frac{\partial\phi}{\partial\boldsymbol{n}} = 0, & \text{on } \partial\Omega
\end{cases}
\tag{10}
$$

Here, $|\nabla\phi|$ denotes the norm of the gradient operator of the level set function ϕ, ensuring the smoothness of the generated contour. $\boldsymbol{n}$ represented as the exterior normal at the boundary of $\partial\Omega$ and $\partial\phi/\partial\boldsymbol{n}$ is the normal derivatives level set function ϕ at the boundary. Eq. (10) was solved using a gradient descent approach with a finite difference scheme. The curvature term $\nabla.\left(\nabla\phi/|\nabla\phi|\right)$ is highly non-linear, leading to high computational complexity. As a result, the segmentation process of the DSS2 model is relatively slow.

Although the DSS2 model includes a constraint distance function designed to capture only the targeted object, it lacks local intensity information, which is crucial for segmenting images with inhomogeneous intensities. The intensity constants in the DSS2 formulation, which approximate the global average of the inner and outer intensities along the contour, may significantly differ from the original image if the intensities inside and outside the contour are not homogeneous. Consequently, the DSS2 model is unable to segment colour images with intensity inhomogeneities.

2.3 Selective local image fitting (SLIF) model

In this study, the segmentation of brain abnormalities in both colour and greyscale MRI images was performed using the Selective Local Image Fitting (SLIF) model introduced by [22]. This model was developed by integrating the concept of local image fitting energy from the Local Image Fitting (LIF) model, proposed by [23], and the distance fitting term from the Distance Selective Segmentation 2 (DSS2)

model, proposed by [24], into a variational energy functional within a vector-valued (colour) framework, which can be defined as follows (Eq. (11)):

$$\min_{\phi} \left\{ E_{\varepsilon}^{SLIF}(\phi) = \frac{1}{2} \int_{\Omega} \frac{1}{N} \sum_{i=1}^{N} \left| u^i - n_1^i H_{\varepsilon}(\phi) - n_2^i (1 - H_{\varepsilon}(\phi)) \right|^2 dxdy \right.$$
$$\left. + \int_{\Omega} \theta H_{\varepsilon}(\phi) L_d(x, y) dxdy \right\}, \tag{11}$$

where the first term is the LIF energy in the colour framework and the second term is the distance fitting term. In the first term, the functions $n_1^i(\phi) = mean\left(u^i \in \left(\{(x, y) \in \Omega \mid \phi(x, y) > 0\} \cap K_{\sigma}(x, y)\right)\right)$ and $n_2^i(\phi) = mean\left(u^i \in \left(\{(x, y) \in \Omega \mid \phi(x, y) < 0\} \cap K_{\sigma}(x, y)\right)\right)$ are the mean intensities of the interior and exterior within certain local areas, which are vital to segment intensity inhomogeneity images. $K_{\sigma}(x, y)$ is a Gaussian window that has been reduced with a specified standard deviation σ and size of $(4\omega+1) \times (4\omega+1)$, where ω is the largest integer less than σ. On the other hand, $H_{\varepsilon}(\phi)$ is the regularised form of the Heaviside function such that $H_{\varepsilon}(\phi) = 0.5\left(1 + (2/\pi) \arctan(\phi/\varepsilon)\right)$.

The second term, θ is the area parameter used to restrict only a targeted object. If the targeted region of interest is close to its adjacent region, the value of θ should be larger. Conversely, a smaller value of θ is needed to segment a distinct object. Additionally, the function $L_d(x, y)$ is defined as in Eq. (5). Here, the user inputs a set of geometrical initial markers β interactively using the 'roipoly' function in MATLAB software. The markers must be near the intended object border. To construct a valid initial polygon, the user must input at least three initial markers. The 'roipoly' function generates a binary image mask to be used in the initialisation process of the SLIF model, where pixels inside the region of interest (ROI) are set to 1 and pixels outside the ROI are set to 0.

To solve the energy functional in Eq. (11), the Euler-Lagrange equation is derived and defined as follows in Eq. (12):

$$-\delta_{\varepsilon}(\phi) \left[\frac{1}{N} \sum_{i=1}^{N} \left(u^i - n_1^i H_{\varepsilon}(\phi) - n_2^i (1 - H_{\varepsilon}(\phi)) \right) \left(n_1^i - n_2^i \right) - \theta L_d \right] = 0. \tag{12}$$

The well-known gradient descent scheme is utilised to solve Eq. (12) numerically. Subsequently, the following gradient descent flow is obtained (Eq. (13)):

$$\frac{\partial \phi}{\partial t} = \frac{\partial E_{\varepsilon}^{SLIF}}{\partial \phi} = \delta_{\varepsilon}(\phi) \left[\frac{1}{N} \sum_{i=1}^{N} \left(u^i - u^{LFI^i} \right) \left(n_1^i - n_2^i \right) - \theta L_d \right], \tag{13}$$

where $u^{LFI^i} = n_1^i H_{\varepsilon}(\phi) - n_2^i (1 - H_{\varepsilon}(\phi))$. As for processing the greyscale image, the gradient descent flow of the SLIF model in Eq. (13) will be as follows (Eq. (14)):

$$\frac{\partial \phi}{\partial t} = \frac{\partial E_\varepsilon^{SLIF}}{\partial \phi} = \delta_\varepsilon(\phi)\Big[\big(u - u^{LFI}\big)\big(n_1 - n_2\big) - \theta L_d\Big].$$

(14)

To guarantee the segmentation curve's smoothness, Eq. (13) and Eq. (14) are convolved with a Gaussian function $G_\varsigma = e^{-\left(x^3 + y^2\right) \div 2\varsigma^2}$, with a standard deviation $\varsigma = 0.45$. This technique incurs less computational time compared to the traditional total variation term [22]. The main objective of this paper is to evaluate the effectiveness of the SLIF model in segmenting brain abnormalities specifically in colour MRI images. We focus on colour images because they provide more detailed information, which is crucial for accurately identifying abnormal regions that may be difficult to distinguish in greyscale images due to intensity inhomogeneity. Although greyscale images are included in our study, they are primarily used for comparison to demonstrate the advantages of incorporating colour information. The SLIF model was chosen over existing models like LIF and DSS2 because it is specifically designed to handle colour images and selectively segment regions of interest. Unlike LIF, which is limited to greyscale images, and DSS2, which lacks local intensity fitting, SLIF's ability to manage both colour data and intensity variations makes it the most suitable model for this task.

3.   METHODOLOGY

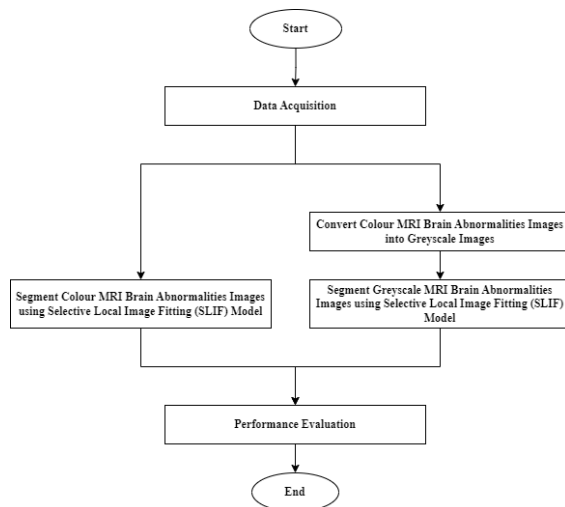This section describes the research framework as outlined in the flow chart in Fig. 1.

Fig. 1. Research framework

As shown in Fig. 1, the research methodology process begins with acquiring 30 colour MRI brain abnormality images, which are then converted into a greyscale format for comparison purposes. The decision to use 30 images aligns with previous related studies [18, 27]. Following this, both the original colour images and the converted greyscale images undergo brain abnormalities segmentation using the Selective Local Image Fitting (SLIF) model. After the segmentation process, the performance of the SLIF model on both colour and greyscale MRI brain images is evaluated and compared, specifically in terms of accuracy and efficiency. The subsequent subsection delves into each of these processes in detail.

3.1 Data acquisition

To ensure the robustness and reliability of the segmentation results, 30 colour MRI brain abnormality images were obtained from two distinct datasets. This approach aimed to minimise potential bias and variability that may arise from relying solely on one dataset. Initially, 15 colour MRI images from patients with lower-grade gliomas (LGG) and their benchmarks, provided in TIFF format, were acquired from [28] and originally sized at 256×256 pixels. Subsequently, another 15 MRI meningioma images and their benchmarks were obtained from the Figshare brain MRI dataset by [29], available in PNG format with dimensions of 512×512 pixels. Notably, the original meningioma MRI images were in greyscale. However, for this study, green meningioma MRI images were employed, following the approach outlined by [5].

The rationale behind using green meningioma images lies in the fact that the green colour mapping reduces the visibility of the background, thereby enhancing the prominence of the meningioma tumour, resulting in better segmentation accuracy compared to the greyscale counterpart [5]. However, the efficacy of green colour mapping has only been validated by non-variational deep learning models. In this study, we are interested in testing its effectiveness in conjunction with the variational active contour model, specifically using the Selective Local Image Fitting (SLIF) model. Furthermore, the selection of both datasets is due to their convenient accessibility and immediate availability. All 30 images were resized to 128×128 pixels to enhance computational efficiency. Bilinear interpolation resizes the image by averaging the nearest four pixels, creating smooth transitions. This preserves important features, like edges and textures, ensuring the resized image maintains its quality for accurate segmentation results [30].

3.2 Convert colour MRI brain abnormalities images into greyscale images

By converting the colour MRI brain images to greyscale, this study aims to assess whether the removal of colour information impacts the segmentation accuracy and efficiency of the variational active contour model. The 'rgb2gray' function in MATLAB software has been implemented to convert colour RGB images to greyscale. The 'rgb2gray' function transforms RGB (colour) images into greyscale by discarding saturation and hue details while preserving luminance [31]. This can be expressed by the following Eq. (15):

$$u = \sum_{i=1}^{N} \alpha(i) \cdot u^i . \tag{15}$$

Here, $u^i = u^i(x, y)$ is the ith colour image channel on the domain Ω with $i = 1, 2, ..., N$ channels. For colour images, the value of N is three ($u^1 =$ red channel, $u^2 =$ green channel and $u^3 =$ blue channel), whereas for greyscale images, the value of N is one. Thus, $u = u(x, y)$ is the converted greyscale image. α is a vector of weights that represents the relative sensitivity of the human eye to the red, green, and blue colour channels. For the greyscale conversion formula, $\alpha = (0.2989, 0.5870, 0.1140)$, where each value corresponds to the weight for the red, green, and blue channels respectively [32].

3.3 Brain abnormalities segmentation using SLIF model

In this study, the segmentation of brain abnormalities in both colour and greyscale MRI images was performed using the Selective Local Image Fitting (SLIF) model introduced by [22]. To implement the SLIF model, the MATLAB R2021a software was utilised. The central processing unit (CPU) processor used was an AMD Ryzen 7 7735HS with Radeon Graphics, operating at a frequency of 3.20 GHz and accompanied by 16 GB of installed memory (RAM). The program is automatically halted using two

stopping criteria: a value of tolerance $tol = 0.005$ and the maximum number of iterations $maxiter = 3000$. The values for tolerance and maximum number of iterations were selected based on the recommendations outlined by [22] in their original paper. The algorithm provided below outlines the implementation process for the SLIF model:

Step 1: Set the value of parameters and define a set of initial markers β.

Step 2: Determine $L_d(x, y)$ using Eq. (5).

Step 3: Initialise the level set function ϕ such that Γ is the boundary of P.

Step 4: **For** iteration $iter = 1$ to *maxiter* or $\left\| \phi^{m+1} - \phi^m \right\| \div \left\| \phi^m \right\| \le tol$ **do**

Compute $n_1^i\left(\phi^m\right)$ and $n_2^i\left(\phi^m\right)$.

Evolve ϕ based on Eq. (13) for colour and Eq. (14) for the converted greyscale image to get

ϕ^{m+1}.

Regularise ϕ by convolving ϕ^{m+1} with a Gaussian function $G_\varsigma = e^{-\left(x^3 + y^2\right) \div 2\varsigma^2}$.

end for

Step 5: The output ϕ is the ultimate resolution.

3.4   Performance evaluation

To assess and compare the segmentation accuracy, three distinct evaluation metrics were utilised. The first of these is the Dice Similarity Coefficient (DSC), which is mathematically represented as follows (Eq. (16)):

$$DSC = \frac{2TP}{2TP + FP + FN}, \tag{16}$$

where TP represents True Positive (correctly predicted as an abnormality), FP stands for False Positive (incorrectly predicted as an abnormality) and FN corresponds to False Negative (incorrectly predicted as normal) [33]. Subsequently, the Inter-section-over-Union (IoU) metric was employed, which can be defined as follows (Eq. (17)):

$$IoU = \frac{TP}{TP + FP + FN}. \tag{17}$$

The difference between the DSC and the IoU lies in how they penalise over-segmentation and under-segmentation, with the IoU applying greater penalties than the DSC. Both metrics are scored on a scale from 0 to 1. A score of 0 indicates no overlap between the actual and predicted segments, while a score of 1 signifies complete congruence. Therefore, higher DSC and IoU scores reflect superior segmentation accuracy [5].

Furthermore, this study also employed the Matthews correlation coefficient (MCC). The MCC serves as a correlation coefficient between the actual and predicted binary values, providing a result that ranges

from -1 to +1. A score of +1 indicates a perfect prediction, 0 signifies performance equivalent to random guessing, and -1 implies complete discordance between the actual and predicted values. The MCC is calculated using the following formula in Eq. (18):

$$MCC = \frac{(TP \times TN) - (FP \times FN)}{\sqrt{(TP + FP)(TP + FN)(TN + FP)(TN + FN)}} \, . \tag{18}$$

Moreover, this research also evaluated and compared the efficiency of segmenting brain abnormalities in colour and greyscale MRI images by analysing the elapsed processing time. Accurate measurement of elapsed processing time was achieved using the 'tic' and 'toc' MATLAB built-in functions. To ensure the robustness of the results, the experiment was replicated thrice, and the average elapsed processing time $\bar{\tau}$ was calculated.

4.   RESULTS AND DISCUSSION

This section discusses the overall segmentation outcomes for both colour and its converted greyscale MRI brain abnormalities utilising the Selective Local Image Fitting (SLIF) model. Regarding parameter configuration, we maintained a fixed value of epsilon $\varepsilon = 1$, standard deviation $\varsigma = 0.45$, maximum iteration $maxiter = 3000$ and tolerance $tol = 0.005$. However, the values of the parameter area θ and standard deviation σ varied depending on the individual MRI brain images to achieve optimal segmentation results: $\theta = [20, 500]$ and $\sigma = [2, 15]$. Table 1 presents all 30 colour brain abnormalities MRI images used in this study.

As illustrated in Table 1, images 1 to 15 are colour MRI images from patients with lower-grade gliomas (LGG), while images 16 to 30 are green meningioma MRI images. Each image is annotated with a set of initial markers indicating the targeted brain abnormalities to be segmented. For a fair comparison, the coordinates of the initial markers were kept consistent for both the colour images and their converted greyscale counterparts. Table 2 illustrates the visual comparison of segmentation results for four colour brain MRI images from Table 1 using the SLIF model.

Based on Table 2, the images in the first column are colour MRI brain images with initial markers. As shown in the second column, the initial markers are connected to construct an initial contour for the initialization process. The third column displays benchmark images validated by experts. The binary segmentation results for the colour MRI brain images, generated using the SLIF model, are shown in the fourth column. Meanwhile, the binary segmentation results for the converted greyscale counterparts are presented in the fifth column. By visual inspection, the SLIF model appears to segment brain abnormalities comparably well in both the colour images and their converted greyscale versions. To quantitatively assess performance, Table 3 presents a comparison of the numerical segmentation results obtained from the 30 brain MRI images using the SLIF model. The comparison includes four key evaluation metrics: Dice Similarity Coefficient (DSC), Intersection-over-Union (IoU), Matthews Correlation Coefficient (MCC), and average elapsed processing time $\bar{\tau}$.
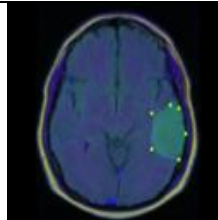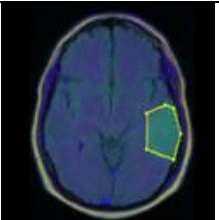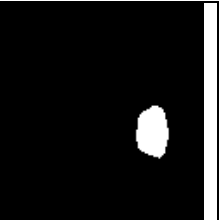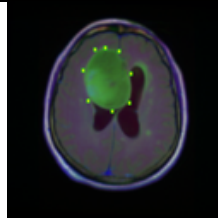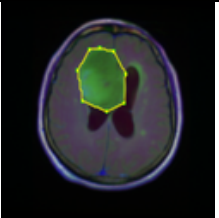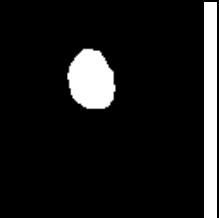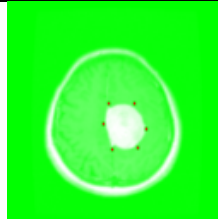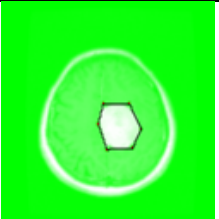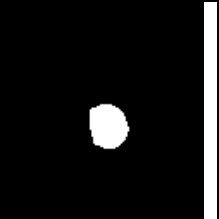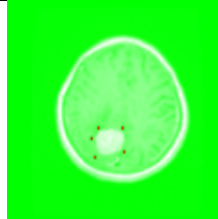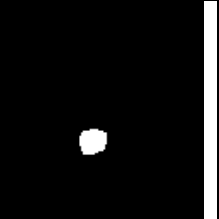
In Table 3, it's evident that across all 30 brain MRI images, the DSC, IoU, and MCC values are consistently higher for colour images compared to their converted greyscale counterparts when using the SLIF model. On average, the colour images achieved a DSC of 0.9282, an IoU of 0.8669, and an MCC of 0.9281, whereas the greyscale images achieved a DSC of 0.9171, an IoU of 0.8481 and an MCC of 0.9178. Consequently, the percentage differences for DSC, IoU, and MCC are approximately 1.21%, 2.22%, and 1.12%, respectively. This disparity suggests that colour images provide supplementary information, thereby

Table 1. Colour brain abnormalities MRI images with initial markers
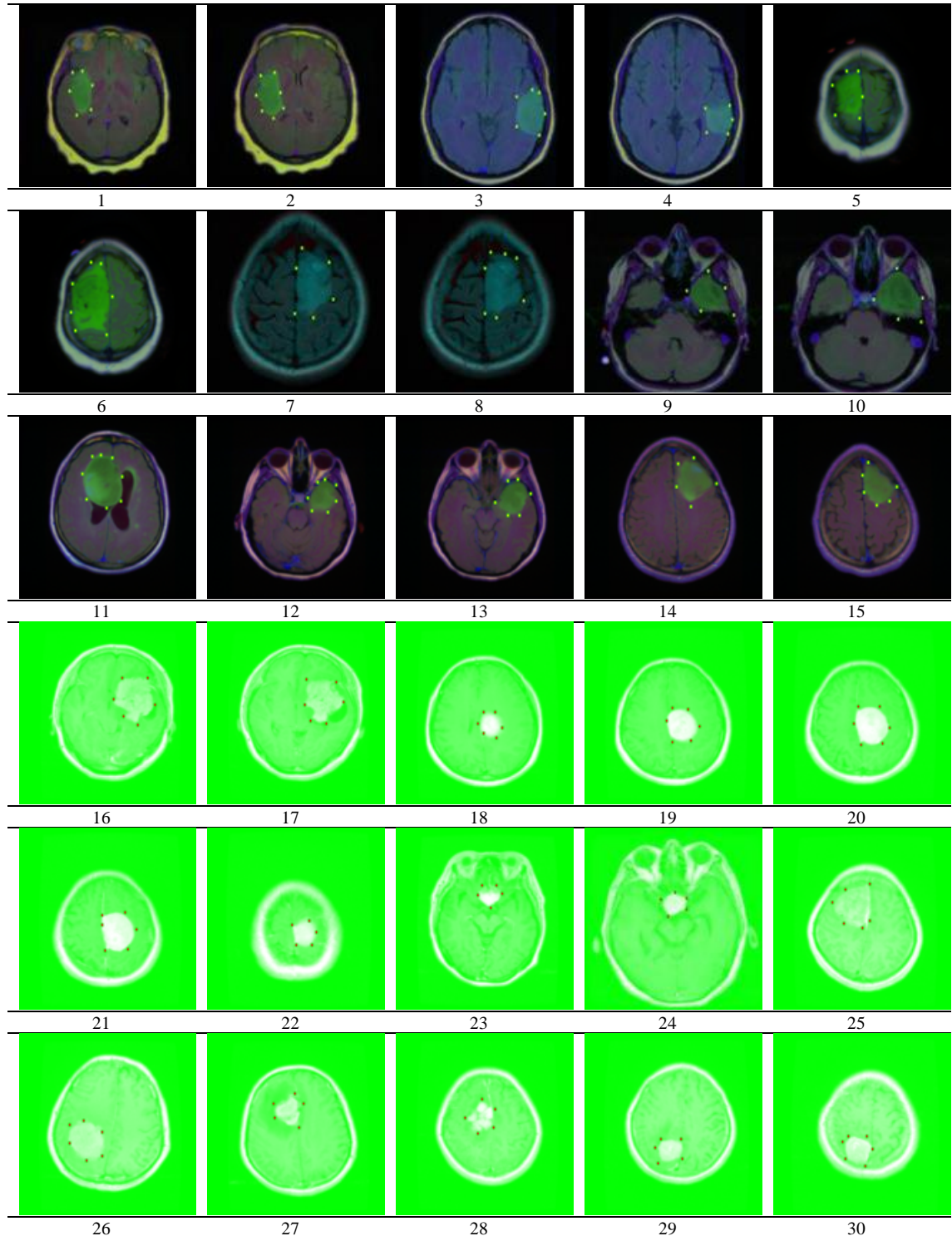
enhancing the model's capacity to distinguish between targeted brain abnormalities and surrounding tissue. Therefore, the utilization of colour MRI leads to a more precise delineation of abnormalities, underscoring the advantages of employing colour imaging in segmentation tasks.

Table 2. Comparison of the segmentation results using the SLIF model

Brain MRI Image with Initial Markers	Brain MRI Image with Initial Contour	Benchmark	Segmentation Result (Colour)	Segmentation Result (Converted Greyscale)
3	3a	3b	3c	3d
11	11a	11b	11c	11d
20	20a	20b	20c	20d
29	29a	29b	29c	29d

When processing colour images, the SLIF model treats the image as a vector-valued function, where each pixel contains three values corresponding to the RGB channels. The model processes each channel independently by applying the same variational segmentation framework to all three channels. This approach allows the segmentation to account for colour information during the curve evolution process. The final segmentation result is obtained by combining the information from all three channels. This results in a more accurate delineation of the abnormal regions compared to grayscale images, which lack this additional colour information.

In addition to the observed improvements in segmentation accuracy, it is noteworthy to consider the computational aspect. On average, processing a single-colour image took 3.1431 seconds, while a greyscale

image required 2.2561 seconds when using the SLIF model. Despite the slight increase in processing time for colour images, the corresponding enhancement in segmentation accuracy justifies this trade-off. Overall, these findings highlight the promising role of colour MRI in enhancing diagnostic accuracy and improving clinical decision-making, particularly in the realm of brain cancer detection applications.

Table 3. Comparison of the segmentation results using the SLIF model

Brain MRI Image	SLIF Model (Colour Image)				SLIF Model (Converted Greyscale Image)			
	DSC	IoU	MCC	$\bar{\tau}$	DSC	IoU	MCC	$\bar{\tau}$
1	0.9258	0.8619	0.9268	3.0555	0.9139	0.8414	0.9155	2.2571
2	0.9106	0.8359	0.9121	3.0732	0.9015	0.8207	0.9036	2.2422
3	0.8800	0.7857	0.8830	3.5065	0.8778	0.7822	0.8810	1.7311
4	0.8793	0.7846	0.8835	3.4337	0.8759	0.7793	0.8805	1.6781
5	0.8879	0.7985	0.8891	2.0629	0.8528	0.7434	0.8555	1.8735
6	0.9351	0.8781	0.9330	3.4984	0.9280	0.8658	0.9257	2.3184
7	0.9292	0.8678	0.9264	5.7623	0.9309	0.8707	0.9282	3.2151
8	0.9460	0.8975	0.9430	2.3553	0.9434	0.8929	0.9402	2.1408
9	0.9227	0.8564	0.9216	2.1668	0.9139	0.8414	0.9137	1.9994
10	0.9571	0.9177	0.9557	2.3673	0.9405	0.8877	0.9388	2.1050
11	0.9318	0.8724	0.9306	2.1710	0.9293	0.8679	0.9280	1.9907
12	0.9365	0.8806	0.9359	2.2268	0.9373	0.8820	0.9363	2.0181
13	0.9189	0.8500	0.9200	2.9236	0.9008	0.8195	0.9033	2.1567
14	0.8837	0.7916	0.8856	2.8946	0.8941	0.8084	0.8953	2.1910
15	0.8845	0.7930	0.8870	3.3643	0.8937	0.8079	0.8953	2.3542
16	0.9489	0.9027	0.9475	2.5381	0.9204	0.8525	0.9201	2.0705
17	0.9352	0.8784	0.9335	2.1908	0.9288	0.8670	0.9279	2.0465
18	0.9051	0.8267	0.9077	2.9248	0.8828	0.7902	0.8876	2.3409
19	0.9701	0.9420	0.9695	2.2512	0.9599	0.9229	0.9594	2.1519
20	0.9714	0.9443	0.9706	2.2728	0.9680	0.9380	0.9671	2.1646
21	0.9701	0.9420	0.9692	2.2582	0.9720	0.9456	0.9712	2.1001
22	0.9451	0.8960	0.9444	2.2199	0.9083	0.8320	0.9096	2.1082
23	0.8919	0.8049	0.8911	8.6921	0.8897	0.8012	0.8894	3.4989
24	0.9434	0.8929	0.9432	2.1303	0.9421	0.8906	0.9428	2.0242
25	0.9462	0.8978	0.9445	2.9016	0.9350	0.8779	0.9339	2.0865
26	0.9505	0.9057	0.9491	2.2996	0.8876	0.7980	0.8905	2.0414
27	0.9131	0.8333	0.9134	3.3514	0.9091	0.8333	0.9109	2.5362
28	0.9369	0.8813	0.9374	8.9381	0.9219	0.8551	0.9236	3.9755
29	0.9476	0.9005	0.9483	2.2887	0.9349	0.8778	0.9361	2.2550
30	0.9403	0.8873	0.9406	2.1720	0.9195	0.8511	0.9213	2.0118
Average	**0.9282**	**0.8669**	**0.9281**	**3.1431**	**0.9171**	**0.8481**	**0.9178**	**2.2561**

5. CONCLUSION

In conclusion, this study investigated the effectiveness of the SLIF model in segmenting brain abnormalities in colour MRI images compared to converted greyscale counterparts. To ensure the strength and dependability of the segmentation outcomes, 30 images of colour MRI brain abnormalities were sourced from two separate datasets: 15 colour MRI images with lower-grade gliomas (LGG) and 15 colour MRI meningioma images. This method was employed to mitigate potential biases and variances that could occur solely depending on one dataset. Experimental results demonstrated that while both colour and converted greyscale images achieved high segmentation accuracy when using the SLIF model, colour MRI images

exhibited slightly better performance across key evaluation metrics, including Dice Similarity Coefficient (DSC), Intersection-over-Union (IoU) and Matthews Correlation Coefficient (MCC). Additionally, colour imaging provided supplementary information, enhancing the model's capacity to delineate abnormalities precisely. However, it is essential to note the slight increase in processing time for colour images, suggesting a trade-off between accuracy and efficiency.

Further research is needed to validate these findings on larger and more diverse datasets, covering various types of brain abnormalities and clinical scenarios. To enhance the segmentation accuracy of the SLIF model in colour MRI brain abnormality images, it can be refined by incorporating image enhancement techniques in colour space as a new fitting term, following the research by [27]. Additionally, since the SLIF model has not been applied to segment text in document-like images, such as old Jawi manuscripts (OJM), future studies could integrate image inpainting techniques from work by [34] into the SLIF formulation to segment Jawi text OJM. Moreover, future work could also extend this study to evaluate the brain abnormalities segmentation accuracy and efficiency of the SLIF model on 3D colour and greyscale MRI images, providing a more comprehensive understanding of the model's performance in three dimensions and potentially leading to further advancements in segmentation techniques and clinical applications.

6.   ACKNOWLEDGEMENTS

7.   CONFLICT OF INTEREST

The authors declare no conflict of interest.

8.   AUTHORS' CONTRIBUTIONS

Akmal Shafiq Badarul Azam: Conceptualisation, methodology, formal analysis, investigation, writing-original draft, and writing-review and editing; **Abdul Kadir Jumaat**: Conceptualisation, methodology, supervision, validation, and writing-review and editing; **Shafaf Ibrahim**: Supervision and writing-review and editing; **Nor Farihah Azman**: Conceptualisation, investigation, and writing-original draft; **Sarah Farhana Zamalik**: Conceptualisation, investigation, and writing-original draft; **Muhammad Zulkhairi Zakariah**: writing-original draft and writing-review and editing.

9.   REFERENCES

[1]   X. Liu, H. Jiang, and X. Wang, "Advances in Cancer Research: Current and Future Diagnostic and Therapeutic Strategies," *Biosensors,* vol. 14, no. 2, p. 100, 2024. [Online]. Available: https://www.mdpi.com/2079-6374/14/2/100.

[2]   F. Bray *et al.*, "Global cancer statistics 2022: GLOBOCAN estimates of incidence and mortality worldwide for 36 cancers in 185 countries," *CA: A Cancer Journal for Clinicians,* vol. 74, no. 3, pp. 229-263, 2024. Available: https://doi.org/10.3322/caac.21834.

[3]   M. J. Holcomb and R. S. Dean, "Brain Abnormalities," in *Encyclopedia of Child Behavior and Development*, S. Goldstein and J. A. Naglieri Eds. Boston, MA: Springer US, pp. 282-284, 2011. Available: https://doi.org/10.1007/978-0-387-79061-9_406.

[4]   S. Nema, A. Dudhane, S. Murala, and S. Naidu, "RescueNet: An unpaired GAN for brain tumor segmentation," *Biomedical Signal Processing and Control,* vol. 55, p. 101641, 2020. Available: https://doi.org/10.1016/j.bspc.2019.101641.

[5]   A. S. B. Azam, A. K. Jumaat, and S. Ibrahim, "Comparison of Various Colorization Techniques for MRI Brain Tumor Segmentation using Convolutional Neural Networks," in *2023 IEEE 8th International Conference on Recent Advances and Innovations in Engineering (ICRAIE),* pp. 1-6, 2023. Available: doi: 10.1109/ICRAIE59459.2023.10468529.

[6]   F. Lateef and Y. Ruichek, "Survey on semantic segmentation using deep learning techniques," *Neurocomputing,* vol. 338, pp. 321-348, 2019. Available: https://doi.org/10.1016/j.neucom.2019.02.003.

[7]   S. A. Abdullah and A. K. Jumaat, "Selective Image Segmentation Models Using Three Distance Functions," *Journal of Information and Communication Technology,* vol. 21, no. 1, pp. 95-116, 2021. Available: doi: 10.32890/jict2022.21.1.5.

[8]   A. B. Yearwood, "A Brief Survey on Variational Methods for Image Segmentation," 2018. [Online].Available:https://www.researchgate.net/publication/323971382_A_Brief_Survey_on_Variational_Methods_for_Image_Segmentation.

[9]   S. Moussa and S. Chouaib, "Brain MRI Segmentation Using a Fast Fuzzy c-means Algorithm," in *2020 4th International Symposium on Informatics and its Applications (ISIA),* pp. 1-6, 2020. Available: doi: 10.1109/ISIA51297.2020.9416540.

[10]   S. V. Aruna Kumar, E. Yaghoubi, and H. Proença, "A Fuzzy Consensus Clustering Algorithm for MRI Brain Tissue Segmentation," *Applied Sciences*, vol. 12, no. 15. Available: doi: 10.3390/app12157385.

[11]   M. I. Sharif, J. P. Li, M. A. Khan, and M. A. Saleem, "Active deep neural network features selection for segmentation and recognition of brain tumors using MRI images," *Pattern Recognition Letters,* vol. 129, pp. 181-189, 2020. Available: https://doi.org/10.1016/j.patrec.2019.11.019.

[12]   D.-T. Nguyen, T.-T. Tran, and V.-T. Pham, "Attention U-Net with Active Contour Based Hybrid Loss for Brain Tumor Segmentation," in *Soft Computing: Biomedical and Related Applications*, N. H. Phuong and V. Kreinovich Eds. Cham: Springer International Publishing, pp. 35-45, 2021. Available: https://doi.org/10.1007/978-3-030-76620-7_3

[13]   T. C. Saibin, A. K. b. Jumaat, and M. Yusoff, "Variational Fuzzy Energy Active Contour Models for Image Segmentation: A Review," in *2023 4th International Conference on Artificial Intelligence and Data Sciences (AiDAS),* pp. 293-297, 2023. Available: doi: 10.1109/AiDAS60501.2023.10284601.

[14]   A. K. Jumaat and K. Chen, "A reformulated convex and selective variational image segmentation model and its fast multilevel algorithm," *Numerical Mathematics,* vol. 12, no. 2, pp. 403-437, 2019. Available: doi: 10.4208/nmtma.OA-2017-0143.

[15]   X. Meng, W. Gu, Y. Chen, and J. Zhang, "Brain MR image segmentation based on an improved active contour model," *PLOS ONE,* vol. 12, no. 8, p. e0183943, 2017. Available: doi: 10.1371/journal.pone.0183943.

[16]   S. Tripathi, R. S. Anand, and E. Fernandez, "Segmentation of Brain Lesions in MR Images," in *2018 International Conference on Recent Innovations in Electrical, Electronics & Communication Engineering (ICRIEECE),* pp. 1684-1688, 2018. Available: doi: 10.1109/ICRIEECE44171.2018.9009332.

[17]   N. A. Ghani, A. K. Jumaat, R. Mahmud, M. A. Maasar, F. A. Zulkifle, and A. M. Jasin, "Breast Abnormality Boundary Extraction in Mammography Image Using Variational Level Set and Self-Organizing Map (SOM)," *Mathematics,* vol. 11, no. 4, 2023. Available: doi: 10.3390/math11040976.

[18]   M. S. Mazlin, A. K. Jumaat, and R. Embong, "Saliency-based variational active contour model for image with intensity inhomogeneity," *Indonesian Journal of Electrical Engineering and Computer*

Science, vol. 32, no. 1, pp. 206-215, 2023. Available: http://doi.org/10.11591/ijeecs.v32.i1.pp206-215.

[19]	L. Burrows, J. Patel, A. I. Islim, M. D. Jenkinson, S. J. Mills, and K. Chen, "A semi-automatic segmentation method for meningioma developed using a variational approach model," *The Neuroradiology Journal,* vol. 37, no. 2, pp. 199-205, 2024. Available: doi: 10.1177/19714009231224442.

[20]	N. Badshah, H. Atta, S. I. A. Shah, S. Attaullah, N. Minallah, and M. Ullah, "New Local Region Based Model for the Segmentation of Medical Images," *IEEE Access,* vol. 8, pp. 175035-175053, 2020. Available: doi: 10.1109/ACCESS.2020.3026143.

[21]	A. Nor Farihah *et al.*, "Digital Medical Images Segmentation by Active Contour Model based on the Signed Pressure Force Function," *Journal of Information and Communication Technology,* vol. 23, no. 3, pp. 393-419, 2024. Available: doi: 10.32890/jict2024.23.3.2.

[22]	A. S. B. Azam, A. K. Jumaat, M. A. Maasar, M. F. Laham, and N. N. A. Rahman, "Local Image Fitting-Based Active Contour for Vector-Valued Images," *Indonesian Journal of Electrical Engineering and Computer Science,* vol. 32, no. 1, pp. 227-235, 2023. Available: doi: 10.11591/ijeecs.v32.i1.pp227-235

[23]	K. Zhang, H. Song, and L. Zhang, "Active contours driven by local image fitting energy," *Pattern Recognition,* Article vol. 43, no. 4, pp. 1199-1206, 2010, doi: 10.1016/j.patcog.2009.10.010.

[24]	N. A. S. M. Ghani and A. K. Jumaat, "Selective Segmentation Model for Vector-Valued Images," *Journal of Information and Communication Technology,* vol. 21, no. 2, pp. 149-173, 2022. Available: doi: 10.32890/jict2022.21.2.1.

[25]	S. Biswas and R. Hazra, "A level set model by regularizing local fitting energy and penalty energy term for image segmentation," *Signal Processing,* vol. 183, p. 108043, 2021. Available: doi: 10.1016/j.sigpro.2021.108043.

[26]	J. Fang, H. Liu, J. Liu, H. Zhou, L. Zhang, and H. Liu, "Fuzzy region-based active contour driven by global and local fitting energy for image segmentation," *Applied Soft Computing,* vol. 100, p. 106982, 2021. Available: doi: 10.1016/j.asoc.2020.106982.

[27]	M. S. Mazlin, A. K. Jumaat, and R. Embong, "Absorbing Markov chain saliency driven active contour model for digital image boundary extraction," *ESTEEM Academic Journal,* vol. 19, pp. 86-98, 2023. [Online]. Available: https://ir.uitm.edu.my/id/eprint/85879.

[28]	M. Buda, A. Saha, and M. A. Mazurowski, "Association of genomic subtypes of lower-grade gliomas with shape features automatically extracted by a deep learning algorithm," *Computers in Biology and Medicine,* vol. 109, pp. 218-225, 2019. Available: doi: 10.1016/j.compbiomed.2019.05.002.

[29]	J. Cheng. *Brain Tumor Dataset (Version 5).* figshare, doi: 10.6084/m9.figshare.1512427.v5.

[30]	P. Parsania and P. Virparia, "A Comparative Analysis of Image Interpolation Algorithms," *IJARCCE,* vol. 5, pp. 29-34, 2016. Available: doi: 10.17148/IJARCCE.2016.5107.

[31]	I. The MathWorks. "Convert RGB image or Colormap to Grayscale - MATLAB RGB2Gray." https://www.mathworks.com/help/matlab/ref/rgb2gray.html (accessed 1 June 2024, 2024).

[32]	E. Cordelli and P. Soda, "Color to grayscale staining pattern representation in IIF," in *24th International Symposium on Computer-Based Medical Systems (CBMS)*, pp. 1-6, 2011. Available: doi: 10.1109/CBMS.2011.5999110.

[33]	A. S. B. Azam, A. A. Malek, A. S. Ramlee, N. D. S. M. Suhaimi, and N. Mohamed, "Segmentation of Breast Microcalcification Using Hybrid Method of Canny Algorithm with Otsu Thresholding and 2D Wavelet Transform," *2020 10th IEEE International Conference on Control System, Computing and Engineering (ICCSCE),* pp. 91-96, 2020. Available: doi: 10.1109/ICCSCE50387.2020.9204950.

[34]	N. N. Zainal, N. F. Mohammad Yuri, and A. K. Jumaat, "Restoration of old malay jawi manuscripts using mumford-shah and bertalmio inpainting models," *Malaysian Journal of*

Computing (MJoC), vol. 7, no. 1, pp. 1047-1055, 2022. [Online]. Available: https://ir.uitm.edu.my/id/eprint/60841.